

A Phenomenological Causal-Response Model for Galactic Rotation Curves with Global Parameters

Jonathan Washburn,¹ Megan Simons,¹ and Elshad Allahyarov^{1, 2, 3, 4, *}

¹*Recognition Science Institute, Austin, Texas, USA*

²*Institut für Theoretische Physik II: Weiche Materie, Heinrich-Heine Universität Düsseldorf, Universitätstrasse 1, 40225 Düsseldorf, Germany*

³*Theoretical Department, Joint Institute for High Temperatures, Russian Academy of Sciences (IVTAN), 13/19 Izhorskaya street, Moscow 125412, Russia*

⁴*Department of Physics, Case Western Reserve University, Cleveland, Ohio 44106-7202, United States*

We present a phenomenological causal-response model for galaxy rotation curves, formulated as a retarded linear-response modification of Newtonian gravity with a single memory timescale $\tau_* \approx 133$ Myr. The effective acceleration is parameterized as $a_{\text{eff}}(r) = w(r) a_{\text{baryon}}(r)$ with a globally shared weight function $w(r) = 1 + \xi n(r) (a_0/a_{\text{baryon}}(r))^\alpha \zeta(r)$ that approaches $w \rightarrow 1$ in fast/high-acceleration limits, ensuring consistency with Solar System tests. The framework admits a conservative realization via the Caldeira–Leggett formalism. Fitting global parameters once to the SPARC $Q = 1$ sample (99 galaxies) under a strict global-only protocol (no per-galaxy tuning of stellar M/L , distance, or inclination) yields median $\chi^2/N = 1.19$, improving on a global-only MOND baseline ($\chi^2/N = 1.79$) by 33% under identical assumptions. The same global fit reproduces the radial acceleration relation (RAR, scatter $\sigma = 0.13$ dex) and baryonic Tully–Fisher relation (BTFR, slope $\beta \approx 3.5$, scatter $\sigma = 0.18$ dex), predicts systematically stronger enhancement in dwarfs ($w \approx 2.2$) than in spirals ($w \approx 1.5$), and removes the residual trend with gas fraction present in MOND. The model is falsifiable through quantitative predictions for dwarf/spiral enhancement ratios, RAR scatter, and prospective galaxy cluster observations.

Keywords: galaxies: kinematics and dynamics — galaxies: structure — galaxies: rotation curves — dark matter — gravitation — methods: data analysis — galaxies: fundamental parameters — catalogs: SPARC

1

I. INTRODUCTION

2 Galaxy rotation curves have challenged our understanding of gravity for over four decades (Bosma 1981, Rubin & Ford 1970). Across disk galaxies, the observed orbital speed $v(r)$ often remains approximately flat or slowly rising with radius, contrary to the Keplerian decline $v \propto r^{-1/2}$ expected from Newtonian gravity sourced only by the observed baryons. A flat rotation curve implies an enclosed mass that grows approximately linearly with radius, $M_{\text{enc}} \propto r$, indicating a systematic deficit between observed and predicted mass. Related tensions appear in galaxy clusters (Zwicky 1933) and in the growth of large-scale structure (Planck Collaboration 2020), motivating either additional gravitating matter or a modification of gravitational dynamics.

3 The prevailing Λ CDM (Lambda Cold Dark Matter) paradigm attributes the discrepancy to cold, collisionless dark matter (CDM) interacting only gravitationally (Bertone et al. 2005). On cosmological scales this framework is highly successful, and N-body simulations predict halos with approximately universal density profiles, notably the Navarro–Frenk–White (NFW) form (Navarro et al. 1997), characterized by two free parameters per galaxy: the scale density ρ_s and scale radius r_s . When fitting rotation curves, Λ CDM typically requires 3–5 parameters per galaxy: two halo parameters plus 1–2 stellar mass-to-light ratios M_\star/L , and occasionally distance/inclination adjustments.

4 Despite these successes, CDM faces persistent small-scale tensions: the cusp–core problem (de Blok 2010, Oh et al. 2015), missing satellites (Klypin et al. 1999, Moore et al. 1999), too-big-to-fail (Boylan-Kolchin et al. 2011), and the diversity problem (Bullock & Boylan-Kolchin 2017, Oman et al. 2015). Empirically, galaxy dynamics also exhibit tight scaling regularities. A prominent example is the Radial Acceleration Relation (RAR) (McGaugh et al. 2016), a correlation between the observed centripetal acceleration $a_{\text{obs}}(r) = v_{\text{obs}}^2(r)/r$ and the baryonic Newtonian prediction $a_{\text{baryon}}(r) = v_{\text{baryon}}^2(r)/r$. In the low-acceleration limit, this is often summarized by $a_{\text{obs}} \approx \sqrt{a_0 a_{\text{baryon}}}$, where $a_0 \sim 10^{-10} \text{ m/s}^2$ is an empirical acceleration scale, and more general power-law parameterizations appear in the literature. Despite decades of searches, no dark matter particle has been detected (Aprile et al. 2018, Bertone et al. 2005).

5 Motivated by these tensions, numerous modified-gravity frameworks have been proposed. Modified Newtonian Dynamics (MOND) (Milgrom 1983) introduces a characteristic acceleration scale $a_0 \approx 1.2 \times 10^{-10} \text{ m s}^{-2}$ below which

* elshad.allahyarov@case.edu

TABLE I. Comparison of major approaches to galactic rotation curves. “Params/gal” denotes typical per-galaxy fit parameters in rotation-curve practice. Entries for clusters and cosmology are qualitative (tension vs. success) and refer to standard formulations without additional ad hoc components unless noted.

Theory	Params/gal	GR limit	Rotation curves	Clusters	Cosmology
Λ CDM (NFW)	3–5	Yes	Fit well (3–5 params/gal)	Successful	Successful
MOND	1–3	No	Fit well (1–3 params/gal)	Tension w/o extra components	Needs completion
TeVeS	1–3	Yes	MOND-like fits	Tension w/o extra components	Constrained
$f(R)$ gravity	1–3	Yes (weak)	Not targeted	Model dependent	Successful (some forms)
Massive gravity	1–3	Yes (weak)	Not targeted	Model dependent	Successful (some forms)
Verlinde (2017)	1–2	Yes	Limited	Limited	Limited
Causal response	0	Yes	Global-only (this work)	Not addressed	Not addressed

the effective force law departs from Newtonian behavior. MOND fits many galaxy rotation curves with remarkable economy (Famaey & McGaugh 2012, McGaugh et al. 2016, Sanders & McGaugh 2002) and naturally connects to the baryonic Tully–Fisher relation (BTFR) and the RAR. In practice, rotation-curve analyses typically still involve per-galaxy nuisance freedom (e.g., M_*/L and distance/inclination adjustments), and MOND faces well-known difficulties with galaxy clusters without additional dark components (Angus et al. 2008). Relativistic completions include TeVeS (Bekenstein 2004), while alternative approaches include $f(R)$ gravity (Sotiriou & Faraoni 2010), scalar–tensor theories (Fujii & Maeda 2003), massive gravity (de Rham 2014), and emergent-gravity proposals (Verlinde 2011, 2017).

For orientation, Table I coarsely summarizes how several major approaches address rotation curves, clusters, and cosmology, and how much per-galaxy tuning is typically used in practice.

In this work, we propose a phenomenological *causal-response*(CR) model in which the effective gravitational acceleration is parameterized as $a_{\text{eff}}(r) = w(r) a_{\text{baryon}}(r)$, where $w(r)$ is a globally shared weight function. The key hypothesis is that the enhancement $w(r)$ is controlled primarily by local dynamical time and morphology and can be described by a *single* functional form shared by all galaxies. Operationally, we enforce a strict global-only protocol: all parameters entering $w(r)$ are fit once with no per-galaxy tuning. The weight function $w(r)$ is derived from a retarded linear-response kernel with a characteristic memory timescale τ_* (determined from the global fit, Sec. III). This timescale is constructed to recover Newtonian/General Relativity (GR) behavior in fast-dynamics limits (typically massive spirals) while allowing larger enhancements in slow-dynamics regimes (typically dwarfs).

We test the model on the highest-quality $Q = 1$ subset of the SPARC (Spitzer Photometry & Accurate Rotation Curves) catalog (Lelli et al. 2016) ($N = 99$ galaxies) using a fixed error model and masking protocol applied identically to a global-only MOND baseline. The CR model achieves median $\chi^2/N = 1.19$ versus 1.79 for MOND—a 33% improvement with zero per-galaxy tuning. The fitted model reproduces the RAR and BTFR, predicts systematically stronger enhancement in dwarfs than in spirals, and removes the residual trend with gas fraction present in MOND. As we show in Sec. II 2.2, the power-law form $(a_0/a_{\text{baryon}})^\alpha$ emerges naturally from scale-free response dynamics.

The remainder of the paper is organized as follows. Section II develops the CR framework and fixes the precise meaning of the steady-state gain and weight functions. Section III specifies the globally shared weight function $w(r)$ and its parameterization. Sections IV and V present the SPARC dataset, fitting protocol, and empirical results. Section VI discusses physical interpretation, comparison to alternatives, and quantitative falsification criteria, and Section VII concludes.

II. THEORETICAL FRAMEWORK

2.1. Causal linear-response framework

We model the effective gravitational acceleration using a causal linear-response framework in which $a_{\text{eff}}(t, r)$ depends on the instantaneous baryonic acceleration $a_{\text{baryon}}(t, r)$ and its past history through a memory kernel:

$$a_{\text{eff}}(t, r) = a_{\text{baryon}}(t, r) + \int_{-\infty}^t \Gamma(t - t', r) a_{\text{baryon}}(t', r) dt' \quad (1)$$

where $\Gamma(\tau, r)$ is the kernel and $\tau = t - t'$ is the lag. For the kernel we adopt an exponential form with single memory

60 timescale τ_* ,

$$61 \quad \Gamma(\tau > 0, r) = \frac{w_{\text{steady}}(r) - 1}{\tau_*} e^{-\tau/\tau_*}, \quad \Gamma(\tau < 0, r) = 0 \quad (2)$$

62 Here $w_{\text{steady}}(r)$ is the steady-state response gain, and the prefactor ensures the correct long-time limit.

63 Taking the Fourier transform of Eq. (1), we obtain the frequency-domain relation:

$$64 \quad a_{\text{eff}}(\omega, r) = H(i\omega, r) a_{\text{baryon}}(\omega, r) \quad (3)$$

65 with transfer function

$$66 \quad H(i\omega, r) = 1 + \int_0^\infty \Gamma(\tau, r) e^{-i\omega\tau} d\tau = 1 + \frac{w_{\text{steady}}(r) - 1}{1 + i\omega\tau_*} \quad (4)$$

67 The real part of the transfer function gives the enhancement factor,

$$68 \quad C(\omega, r) \equiv \text{Re}[H(i\omega, r)] = 1 + \frac{w_{\text{steady}}(r) - 1}{1 + \omega^2\tau_*^2} \quad (5)$$

69 which interpolates between two limits: at low frequency ($\omega\tau_* \ll 1$), $C \rightarrow w_{\text{steady}}(r)$ as the memory fully develops;
70 at high frequency ($\omega\tau_* \gg 1$), $C \rightarrow 1$ recovering instantaneous Newtonian response, ensuring consistency with Solar
71 System tests where dynamical times are much shorter than τ_* .

72 For quasi-steady circular orbits with angular frequency $\omega_{\text{dyn}}(r) \equiv v(r)/r$, galactic systems typically have orbital
73 periods $T_{\text{dyn}} \sim 100\text{--}300$ Myr, comparable to the fitted memory timescale τ_* (Sec. III), giving $\omega_{\text{dyn}}\tau_* \sim 0.5\text{--}1.5$. We
74 define the response gain used in rotation-curve fits as:

$$75 \quad w(r) \equiv C(\omega_{\text{dyn}}(r), r) = 1 + \frac{w_{\text{steady}}(r) - 1}{1 + \omega_{\text{dyn}}^2(r)\tau_*^2} \quad (6)$$

76 This closes the kernel-to-fit connection: the underlying response is frequency-dependent, but rotation-curve fits use
77 the orbital gain $w(r)$ evaluated at ω_{dyn} rather than the zero-frequency limit. Figure 1 illustrates the memory kernel
78 $\Gamma(\tau)$ and response function $C(\omega)$.

79 2.2. Phenomenological ansatz and weight function

80 The causal linear-response formalism yields a phenomenological ansatz for the effective gravitational acceleration,

$$81 \quad a_{\text{eff}}(r) = w(r) a_{\text{baryon}}(r) \quad (7)$$

82 For circular orbits with $a(r) = v^2(r)/r$, this implies the working equation for rotation-curve fits:

$$83 \quad v_{\text{eff}}^2(r) = w(r) v_{\text{baryon}}^2(r) \quad (8)$$

84 In fast/high-acceleration regimes (short dynamical times), $w \rightarrow 1$ recovers Newtonian gravity and ensures consistency
85 with Solar System tests. In slow/low-acceleration regimes (long dynamical times), $w > 1$ provides the empirically
86 required boost.

87 We parameterize $w(r)$ as a power law in the local acceleration (Metzler & Klafter 2000, Podlubny 1999, Samko et
88 al. 1993),

$$89 \quad w(r) - 1 \propto \left(\frac{a_0}{a_{\text{baryon}}(r)} \right)^\alpha \quad (9)$$

90 where a_0 is a characteristic acceleration scale and $0 < \alpha < 1$ is the power-law exponent. Using the orbital time
91 $T_{\text{dyn}}(r) = 2\pi r/v(r)$ and defining a reference radius r_0 where the acceleration equals a_0 , the enhancement can be
92 written as

$$93 \quad w(r) - 1 \propto \left(\frac{T_{\text{dyn}}(r)}{\tau_*} \right)^{2\alpha}, \quad \tau_* = \sqrt{\frac{2\pi r_0}{a_0}} \quad (10)$$

94 The microscopic origin of this power-law form remains open. Possibilities include coupling to a continuum of gravitational modes (Appendix B), nonlocal field propagation, or emergent spacetime response.

96 **2.3. Comparison baseline: Modified Newtonian Dynamics (MOND)**

97 For comparison we use a global-only MOND baseline (Famaey & McGaugh 2012, McGaugh et al. 2016, Milgrom
98 1983), which replaces the Newtonian acceleration-mass relation with a low-acceleration modification governed by a
99 universal scale a_0 ,

100
$$\mu(x) a_{\text{MOND}}(r) = a_{\text{baryon}}(r) \quad (11)$$

101 Here $x \equiv a_{\text{MOND}}/a_0$ is the dimensionless acceleration ratio, $a_{\text{MOND}}(r)$ is the MOND-modified gravitational acceleration,
102 and $a_{\text{baryon}}(r)$ is the Newtonian acceleration computed from the observed baryons. The interpolation function
103 $\mu(x) = x/(1+x)$ satisfies $\mu(x) \rightarrow 1$ for $x \gg 1$ (high-acceleration Newtonian regime, inner disk), and $\mu(x) \rightarrow x$ for
104 $x \ll 1$ (deep-MOND regime, outer disk).

105 The baryonic acceleration $a_{\text{baryon}}(r)$ is computed from the observed mass distribution as a component sum:

106
$$a_{\text{baryon}}(r) = a_{\text{disk}}(r) + a_{\text{bulge}}(r) + a_{\text{gas}}(r) + a_{\text{dust}}(r) \quad (12)$$

107 using the disk, bulge, and gas decomposition provided by SPARC. This Newtonian baseline is identical for both
108 MOND and our CR model, ensuring a fair comparison.

109 In principle, MOND introduces a_0 as a single global parameter. However, in practice, rotation-curve analyses
110 typically include additional per-galaxy degrees of freedom: stellar mass-to-light ratios M/L (1–2 parameters per
111 galaxy), distance D and inclination i (sometimes allowed to vary within observational uncertainties), and occasionally
112 external-field effects g_{ext} . Thus, the statement that MOND has “one fit parameter” is true only under a strict global-
113 only protocol: zero per-galaxy freedom, fixing a single M/L ratio for all galaxies, holding D and i to catalog values,
114 and using one global a_0 . We adopt this stringent benchmark for both MOND and our CR model to ensure a fair
115 comparison (Sec. IV).

116 **III. THE CR MODEL**

117 Having established the response formalism (Sec. II), we write the weight function $w(r)$ in Eq. (7) as a product of
118 four factors:

119
$$w(r) = 1 + \xi \cdot n(r) \cdot \left(\frac{a_0}{a_{\text{baryon}}(r)} \right)^\alpha \cdot \zeta(r) \quad (13)$$

120 where ξ captures morphology/gas-fraction dependence, $n(r)$ is a radial profile normalized per galaxy, $(a_0/a_{\text{baryon}})^\alpha$
121 is the acceleration-dependent power-law scaling, and $\zeta(r)$ is a geometric correction for disk thickness. For circular
122 orbits, this yields the working equation for rotation-curve fits:

123
$$v_{\text{eff}}^2(r) = w(r) v_{\text{baryon}}^2(r) = \left[1 + \xi \cdot n(r) \cdot \left(\frac{a_0}{a_{\text{baryon}}(r)} \right)^\alpha \cdot \zeta(r) \right] \cdot v_{\text{baryon}}^2(r) \quad (14)$$

124 where $v_{\text{baryon}}(r)$ is the Newtonian circular velocity from the observed baryonic mass distribution. The model pre-
125 dicted $v_{\text{eff}}(r)$ using global parameters with no per-galaxy tuning, and is compared to the global-only MOND baseline
126 ($v_{\text{MOND}}^2(r) = v_{\text{baryon}}^2(r)/\mu(x)$) using identical data, uncertainties, and masks.

127 **3.1. Complexity factor ξ**

128 We parameterize the complexity factor as:

129
$$\xi = 1 + C_\xi \sqrt{u_b} , \quad f_{\text{gas}} = \frac{M_{\text{gas}}}{M_{\text{baryon}}} \quad (15)$$

130 where $u_b \in \{0, 0.25, 0.5, 0.75, 1\}$ is a binned proxy for the true gas fraction f_{gas} , and C_ξ is a global coefficient. To
131 avoid overfitting, we bin f_{gas} into five quintiles using the 20th, 40th, 60th, and 80th percentiles from the Q=1 sample
132 ($N = 99$). Each galaxy is assigned u_b by quintile before fitting; C_ξ is the only fitted parameter.

133

3.2. Spatial profile $n(r)$

134

We adopt a three-parameter analytic profile:

135

$$n(r) = 1 + A \left[1 - \exp \left(- \left(\frac{r}{r_0} \right)^p \right) \right] \quad (16)$$

136 where $A > 0$ sets the outer-disk amplitude ($n(\infty) = 1 + A$), $r_0 > 0$ is the transition radius, and $p > 0$ controls
 137 sharpness. This satisfies $n(0) = 1$ and approaches a finite asymptote. To prevent $n(r)$ from acting as a hidden
 138 per-galaxy mass rescaling, we enforce a disk-weighted normalization constraint:

139

$$\langle n \rangle_j \equiv \frac{\int_0^\infty n(r) \Sigma_j(r) r dr}{\int_0^\infty \Sigma_j(r) r dr} = 1 \quad (17)$$

140

141 where $\Sigma(r)$ is the observed baryonic surface density. We compute $\langle n \rangle_j$ for each galaxy j and rescale $n(r) \rightarrow n(r)/\langle n \rangle_j$
 before computing the rotation curve.

142

3.3. Geometric correction $\zeta(r)$

143

The geometric correction captures finite disk-thickness effects:

144

$$\zeta(r) = 1 - \frac{h_z}{R_d} \tanh \left(\frac{r}{R_d} \right) \quad (18)$$

145

146 where R_d is the disk scale length (from SPARC) and h_z/R_d is fixed to 0.25. For the inner disk ($r \ll R_d$), $\zeta(r) \approx 1$;
 147 for the outer disk ($r \gg R_d$), $\zeta(r) \rightarrow 0.75$, providing a mild (~25%) suppression at large radii. Sensitivity tests
 (Appendix C) show that varying h_z/R_d by $\pm 50\%$ changes median χ^2/N by less than 0.05.

148

IV. METHODS

149

4.1. SPARC dataset and galaxy classification

150

151 The SPARC (Spitzer Photometry & Accurate Rotation Curves) dataset (Lelli et al. 2016) provides high-quality
 152 rotation curves and photometric measurements for 175 nearby disk galaxies. Each galaxy includes: resolved rotation
 153 curves $v_{\text{obs}}(r)$ from HI 21-cm observations ($\Delta r \sim 0.5\text{--}2$ kpc resolution); Spitzer 3.6 μm surface photometry tracing
 154 old stellar populations; HI surface density profiles; photometric disk/bulge decompositions with stellar mass-to-light
 ratios $M_\star/L_{3.6}$; and catalog distances D , inclinations i , and quality flags $Q \in \{1, 2, 3\}$.

155 Quality flags indicate: $Q = 1$ (best quality: well-determined D , i , R_d , extended rotation curves; $N = 99$); $Q = 2$
 156 (moderate quality: larger uncertainties or coarser sampling; $N = 64$); $Q = 3$ (lower quality: significant geometric
 157 uncertainties or limited coverage; $N = 12$).

158 Galaxies are also classified by maximum rotation velocity v_{max} : dwarfs ($v_{\text{max}} < 80$ km/s; gas-rich, low-mass);
 159 spirals ($80 \leq v_{\text{max}} \leq 200$ km/s; normal disks); massive spirals ($v_{\text{max}} > 200$ km/s; deep potentials, often prominent
 160 bulges). Table II summarizes the distribution. Stellar masses span $M_\star \sim 10^7\text{--}10^{11} M_\odot$. We focus on the $Q = 1$ subset
 161 ($N = 99$); robustness tests on $Q = 1 + 2$ ($N = 163$) are in Appendix E.

TABLE II. Distribution of SPARC galaxies by kinematic type and quality flag Q .

Subset	Dwarf	Spiral	Massive	Total
Total ($N = 175$)	59	78	38	175
$Q = 1$	19	49	31	99
$Q = 2$	30	27	7	64
$Q = 3$	10	2	0	12

162

4.2. Baryonic acceleration computation

We compute the Newtonian baryonic acceleration $a_{\text{baryon}}(r)$ using observed stellar and gas surface densities. Following SPARC methodology, we adopt: a single global stellar mass-to-light ratio $\Upsilon_* \equiv M_*/L_{3.6}$ (fitted globally, best-fit $\Upsilon_* = 1.0$ solar units; Table III); HI gas masses from observed column densities scaled by 1.33 for helium; negligible dust and molecular gas (subdominant in SPARC).

The baryonic circular velocity $v_{\text{baryon}}(r)$ is computed by solving the Poisson equation for the total baryonic mass distribution, yielding $a_{\text{baryon}}(r) = v_{\text{baryon}}^2(r)/r$. We use the thin-disk approximation with numerical integration over observed surface densities; bulge components are treated as spherical (Binney & Tremaine 2008).

Model parameters are fitted simultaneously to the $Q = 1$ sample with zero per-galaxy tuning. We do not adjust M/L , distances D , inclinations i , or any galaxy-specific parameters. The only per-galaxy inputs are catalog observables $(\Sigma(r), f_{\text{gas}}, R_d)$, making each galaxy an independent test.

173

4.3. Error model and observational uncertainties

Rotation curve measurements include statistical errors and additional systematics. We define an effective per-point uncertainty $\sigma_{\text{eff},i,j}$ (data point i in galaxy j) by adding contributions in quadrature:

$$\sigma_{\text{eff},i,j}^2 = \sigma_{\text{obs},i,j}^2 + \sigma_0^2 + (f_{\text{floor}} \cdot v_{\text{obs},i,j})^2 + \sigma_{\text{beam},i,j}^2 + \sigma_{\text{asym},j}^2 \cdot v_{\text{obs},i,j}^2 + \sigma_{\text{turb},i,j}^2 \quad (19)$$

where σ_{obs} is the catalog-reported uncertainty, $\sigma_0 = 10$ km/s is a fixed velocity floor, $f_{\text{floor}} = 0.05$ captures distance/inclination systematics, σ_{beam} models beam-smearing effects, σ_{asym} accounts for asymmetric drift (0.10 for dwarfs, 0.05 for spirals), and σ_{turb} describes turbulence and warp contributions. Detailed functional forms and physical motivations are provided in Appendix A. All hyperparameters are fixed globally and applied identically to both CR and MOND.

182

4.4. Goodness-of-fit metric

We quantify fit quality using per-galaxy chi-squared statistics:

$$\chi_j^2 = \sum_{i=1}^{N_j} \left(\frac{v_{\text{obs},i,j} - v_{\text{model},i,j}}{\sigma_{\text{eff},i,j}} \right)^2 \quad (20)$$

where j is the galaxy index ($M = 99$), i is the radial bin index, N_j is the number of bins (typically 15–25), $v_{\text{obs},i,j}$ is observed velocity, $v_{\text{model},i,j}$ is the model prediction [Eq. (14) for CR or MOND], and $\sigma_{\text{eff},i,j}$ is the effective uncertainty [Eq. (19)].

We define the reduced chi-squared per galaxy:

$$\left(\frac{\chi^2}{N} \right)_j = \frac{\chi_j^2}{N_j} \quad (21)$$

where $(\chi^2/N)_j \approx 1$ indicates a good fit. Our primary metric is the median across galaxies:

$$\text{Median} \left(\frac{\chi^2}{N} \right) = \text{median}_{j=1}^M \left\{ \left(\frac{\chi^2}{N} \right)_j \right\} \quad (22)$$

This metric is robust to outliers (e.g., barred or warped galaxies), gives equal weight to each galaxy regardless of radial sampling, and directly indicates typical fit quality without requiring knowledge of total data points.

194

4.5. Parameter optimization and fitting procedure

The global model parameters $\boldsymbol{\theta} = (\alpha, a_0, C_\xi, A, r_0, p, \Upsilon_*)$ are optimized simultaneously to minimize the median χ^2/N [Eq. (22)] across the $Q=1$ SPARC subset using Differential Evolution (DE) (Price et al. 2005, Storn & Price 1997). DE, a derivative-free global optimizer suitable for non-convex objectives, searches within physically reasonable bounds for each parameter:

$\alpha \in [0.1, 0.9]$, $C_\xi \in [0.01, 0.5]$, $A \in [0.5, 3]$, $r_0 \in [5, 30]$ kpc, $p \in [0.5, 2.0]$, $a_0 \in [10^{-11}, \times 10^{-9}] \text{ m/s}^2$, $\Upsilon_* \in [0.7, 1.3]$. These bounds were chosen to span the physically plausible range.

TABLE III. Global best fit parameters for the CR model.

Quantity	Value	Notes
<i>Model parameters (fitted):</i>		
α	0.389	Dynamical-time exponent
Υ_*	1.0	Fitted globally; best fit $M_*/L_{3.6}$ (single value for entire catalog)
C_ξ	0.298	Morphology coefficient; $\xi = 1 + C_\xi \sqrt{u_b}$
(A, r_0, p)	(1.06, 17.79 kpc, 0.95)	Radial profile $n(r)$ parameters
a_0	1.95×10^{-10} m/s ²	Characteristic acceleration scale (fitted)

TABLE IV. Global-only benchmark on the SPARC Q=1 subset ($N = 99$). The CR model achieves a 33% reduction in median χ^2/N and 19.5% reduction in RMS velocity residuals compared to MOND.

Model	Median χ^2/N	Mean χ^2/N	RMS Residual (km/s)	Outliers ($\chi^2/N > 5$)
CR	1.19	4.1	17.3	26
MOND	1.79	3.6	21.5	23
Improvement	33%	—	19.5%	—

V. RESULTS

We fit the CR model parameters once to the SPARC Q=1 subset (99 galaxies) using differential evolution (Sec. IV 4.5) under strict global-only constraints; all subsequent results use these frozen parameters with no further adjustments. Table III reports the best-fit parameters, achieving median $\chi^2/N = 1.19$. For comparison, we fit MOND under the same protocol: only a_0 is optimized (no per-galaxy adjustments), using identical $\Upsilon_* = 1.0$, error model, and masks. The MOND baseline achieves $a_0^{\text{MOND}} = 1.23 \times 10^{-10}$ m/s² (close to the canonical value $\approx 1.2 \times 10^{-10}$ m/s²) and median $\chi^2/N = 1.79$ (Table IV)—a 33% worse fit than CR.

5.1. Fitted global parameters

The model has seven fitted global parameters optimized simultaneously under strict global-only constraints (Table III). Key results: power-law exponent $\alpha = 0.389$ governs dynamical-time scaling; characteristic acceleration $a_0 = 1.95 \times 10^{-10}$ m/s² (comparable to MOND’s a_0) combines with $r_0 = 17.79$ kpc to yield memory timescale $\tau_* \approx 133$ Myr; complexity coefficient $C_\xi = 0.298$ gives gas-rich dwarfs a $\sim 30\%$ boost over gas-poor spirals; spatial profile parameters $(A, r_0, p) = (1.06, 17.79, 0.95)$ yield outer-disk enhancement $n(\infty) \approx 2$.

5.2. Rotation curve fits and weight function visualization

Figure 4 shows representative rotation curves for four galaxies spanning three orders of magnitude in stellar mass. The CR model (blue) consistently outperforms MOND (red dashed) and Newtonian predictions (green dotted) across this range. Figure 5 shows the inferred weight profiles $w(r)$: dwarfs exhibit stronger enhancement ($w \sim 2.0\text{--}2.5$) across larger radial ranges than massive spirals ($w \approx 1.0\text{--}1.5$, deviating only at $r > 10$ kpc). Figure 8 confirms this morphology dependence: median $w(R_d) \approx 2.2$ for dwarfs ($N = 19$) versus 1.5 for spirals ($N = 80$).

5.3. Empirical scaling relations: RAR and BTFR

The CR model reproduces two key population-level diagnostics without explicit optimization for them. Figure 6 shows the radial acceleration relation (RAR): CR follows the data across four orders of magnitude with scatter $\sigma_{\text{RAR}} = 0.13$ dex (decimal exponent, where 0.13 dex $\approx 35\%$ scatter), performing comparably to MOND.

Figure 7 shows the baryonic Tully–Fisher relation $M_{\text{baryon}} \propto v_{\text{flat}}^\beta$ (Tully & Fisher 1977): CR predicts $\beta = 3.5$ with $\sigma_{\text{BTFR}} = 0.18$ dex, versus MOND’s $\beta = 4.0$ (consistent with Freeman’s law (Freeman 1970); Appendix D). Figure 9 shows the transition radius R_{trans} (where Newtonian deviations exceed 20%) versus v_{flat} : data follow $R \propto v^{3.2}$, CR predicts $R \propto v^{3.34}$, while MOND predicts $R \propto v^{2.0}$.

228

5.4. Outlier analysis and model limitations

229 The CR model identifies 26 galaxies with $\chi^2/N > 5$ (versus 23 for MOND), representing $\sim 25\%$ of the Q=1 sample.
 230 These outliers are included in all reported statistics (including the median $\chi^2/N = 1.19$) and highlight regimes where
 231 the model's assumptions (steady circular motion, axisymmetry, planar geometry) are violated. Table V lists extreme
 232 cases: UGC 2885 ($\chi^2/N = 14.90$) has strong bars inducing non-circular motions; NGC 1560 and NGC 5907 are edge-
 233 on with inclination uncertainties and warps; DDO 126, IC 2574, and NGC 7793 show irregular or non-equilibrium
 234 dynamics. The comparable outlier rate to MOND suggests these are data/physics-complexity cases rather than
 235 failures unique to CR.

TABLE V. Outlier galaxies with $\chi^2/N > 5$. These cases point to specific physical regimes where the model assumptions (axisymmetry, equilibrium, planar geometry) may be violated. Future extensions incorporating 2D velocity fields, non-axisymmetric structures, and non-equilibrium dynamics are expected to improve these fits.

Galaxy	χ^2/N	Type	Primary Issue	Proposed Remedy
UGC 2885	14.90	Massive	Strong bar	2D velocity field
NGC 1560	5.12	Spiral	Edge-on, inclination	Better geometry
NGC 5907	6.21	Spiral	Edge-on + warp	3D geometry model
DDO 126	5.89	Dwarf	Irregular, non-equilibrium	Exclude or model
IC 2574	5.45	Irregular	Complex gas kinematics	Higher resolution
NGC 7793	5.78	Spiral	Recent merger	Exclude or model

236

5.5. Residual analysis and error model validation

237

We assess residuals using the normalized residuals

$$\delta_{i,j} = \frac{v_{\text{obs},i,j} - v_{\text{model},i,j}}{\sigma_{\text{eff},i,j}} \quad (23)$$

239 where $\sigma_{\text{eff},i,j}$ is the effective uncertainty from Eq. (19). Figure 10 summarizes the residual distribution for the Q=1
 240 sample. After excluding outlier galaxies with $\chi^2/N > 5$ (using the same masking and σ_{eff} definition as in the fit), the
 241 normalized residuals have mean $\mu \approx -0.24$ and standard deviation $\sigma \approx 1.11$. A skew-normal fit (red curve) captures
 242 the mild negative skew and provides a visibly better overlay than a Gaussian with mean fixed to the sample average.

243 The Q–Q plot (against the fitted skew-normal reference) shows good agreement in the central range with mild tail
 244 deviations, consistent with a small fraction of complex systems.

245 The negative mean indicates a mild global over-prediction; its magnitude is small relative to the adopted uncer-
 246 tainties and does not affect the relative model ranking.

247 Figure 11 compares the χ^2/N distributions for the CR model and MOND across the Q=1 sample. The CR
 248 distribution is shifted toward lower (better) values, with median 1.19 versus 1.79 for MOND. This demonstrates
 249 consistent improvement of the CR model across the population. The histogram peaks near $\chi^2/N \sim 1$ for CR indicates
 250 that the typical galaxy is well-fitted, while MOND's distribution centered near $\chi^2/N \sim 1.5$ –2 reflects poorer typical
 251 performance.

252

VI. DISCUSSION

253 The CR model achieves median $\chi^2/N = 1.19$ on the SPARC Q=1 subset, a 33% improvement over MOND
 254 ($\chi^2/N = 1.79$) under identical global-only constraints. We now interpret the fitted weight function $w(r)$, compare to
 255 alternative theories, and discuss possible microphysical origins.

256

6.1. Possible microphysical origins

257 The phenomenological weight function $w(r)$ encodes an enhanced gravitational response in systems with long
 258 dynamical times. While the microscopic origin remains open, possible physical framings include: (1) coupling to addi-
 259 tional degrees of freedom producing enhanced low-frequency response analogous to dielectric enhancement (Caldeira

& Leggett 1983) (Appendix B gives a Caldeira–Leggett realization); (2) infrared/quantum modifications to GR generating memory effects (Deser & Woodard 2013); (3) emergent spacetime response from entanglement/thermodynamics (Jacobson 1995, Verlinde 2017); (4) dissipation-modulated response linking gas-fraction dependence to dissipative versus collisionless dynamics.

The sign $w > 1$ (enhancement, not suppression) follows from thermodynamic stability. For a passive, causal single-Debye response $H(i\omega) = 1 + \Delta/(1 + i\omega\tau_*)$ where $\Delta \equiv (w - 1)$, spectral weight non-negativity enforces $\text{Re}H(0) \geq 1$, thus $\Delta \geq 0$. Physically, a passive reservoir stores/returns energy with a lag but cannot reduce entropy or pump energy; negative Δ would require a non-passive (excited) reservoir. The gravitational "reservoir" (whether hidden sector, quantum vacuum, or emergent degrees of freedom) must be in a low-energy state, thermodynamically forcing $w > 1$, analogous to dielectric/permeability/refractive enhancement in condensed matter. We emphasize these are speculative interpretations; the current work establishes only the phenomenological efficacy of the response formalism under strict global-only constraints.

Table VI shows a potential cosmological connection: the fitted $a_0 \approx 1.95 \times 10^{-10} \text{ m/s}^2$ is within a factor of ~ 2 of the Hubble acceleration $a_H = cH_0/2\pi \approx 1.1 \times 10^{-10} \text{ m/s}^2$. This approximate coincidence, also central to MOND, emerges here from pure timescale optimization. However, the derived memory timescale $\tau_* \approx 133 \text{ Myr}$ is characteristic of galactic dynamics, not cosmological scales ($H_0^{-1} \approx 14 \text{ Gyr}$), suggesting the modification is primarily galactic-scale.

TABLE VI. Comparison of acceleration scales.

Quantity	Value (m/s^2)	Source
Fitted a_0	1.95×10^{-10}	This work (global fit)
MOND a_0	1.20×10^{-10}	Standard literature
Cosmological $cH_0/2\pi$	$\sim 1.1 \times 10^{-10}$	Hubble scale

6.2. Relation to MOND, MOND variants, and alternative theories

Table VII summarizes key conceptual differences between CR (retarded linear-response with memory timescale τ_*) and MOND (acceleration-based interpolation with scale a_0).

TABLE VII. Direct comparison of the CR model vs. standard MOND.

Feature	Standard MOND	CR Model
Ontology	Modified Force Law (Non-linear)	Memory Kernel (Linear Response)
Key Scale	Acceleration a_0 (Fundamental)	Timescale τ_* (Emergent from a_0)
Morphology	None (Mass only)	Explicit ($\xi(f_{\text{gas}})$)
Global Parameters	1 (a_0 fixed)	7 (Fitted globally)
Galaxy Parameters	0	0
Performance	Median $\chi^2/N = 1.79$	Median $\chi^2/N = 1.19$
Transition Scaling	$R \propto V^{2.0}$	$R \propto V^{3.34}$ (Fig. 9)
Residuals Trend	Correlated with f_{gas}	Uncorrelated (Flat)

Alternative theories include: (1) AQUAL (Bekenstein & Milgrom 1984) and QUMOND (Milgrom 2010), which provide field-theoretic MOND formulations but retain acceleration-based interpolation, struggle with cluster-scale issues requiring supplementary dark components, and lack natural morphological dependence; (2) Superfluid dark matter (Berezhiani & Khouri 2015), which assumes Bose-Einstein condensation below $T_c \sim 10^{-3} \text{ eV}$ with phonon-mediated forces mimicking MOND, introduces three new particle parameters (m_{DM}, T_c, c_s), requires fine-tuning to match observations across scales, and predicts untested signatures in mergers and cosmology.

The CR framework fundamentally differs: (i) the modification depends on dynamical time T_{dyn} rather than acceleration, naturally explaining why dwarfs ($T_{\text{dyn}} \sim 500 \text{ Myr}, w \sim 2.2$) show stronger effects than spirals ($T_{\text{dyn}} \sim 200 \text{ Myr}, w \sim 1.5$), with a_0 emerging from $\tau_* = \sqrt{2\pi r_0/a_0}$ rather than as a fundamental constant; (ii) morphological dependence $\xi(f_{\text{gas}})$ is built in from physical motivations (dissipation coupling, fluctuation-dissipation theorem; Appendix B), eliminating MOND's systematic f_{gas} residual trend ($\sim 0.1 \text{ dex offset}$); (iii) no new particle species, phase transitions, or hidden sectors are introduced—the modification is purely gravitational/geometric; (iv) the framework is explicitly causal (retarded Green's functions) and admits a conservative realization (Caldeira-Leggett), ensuring thermodynamic consistency. CR achieves superior performance (median $\chi^2/N = 1.19$ vs. MOND's 1.79, 33% improvement) with zero per-galaxy tuning.

294

6.3. Comparison to empirical dark matter profiles

295 Table VIII compares CR to standard dark matter halo fits. Per-galaxy dark matter profiles (Burkert, pseudo-
 296 isothermal, NFW+contraction, core-NFW) achieve $\chi^2/N < 1$ trivially by overfitting with 2–4 free parameters per
 297 galaxy, sacrificing falsifiability. CR’s $\chi^2/N = 1.19$ with zero per-galaxy freedom demonstrates that a constrained,
 298 physically structured functional form captures common regularities—the key distinction between fitting power (adding
 299 parameters) and physical interpretability under constraint.

TABLE VIII. Comparison of empirical rotation curve fits. CR achieves competitive performance with zero per-galaxy tuning.

Model	Params/gal	Median χ^2/N	Falsifiability
Dark Matter Halos:			
Burkert profile	2	0.8	None
Pseudo-isothermal	2	1.0	None
NFW + adiabatic contraction	4	0.9	Weak
Modified Gravity:			
MOND	0	1.79	Strong
QUMOND	0	1.65	Moderate
CR (this work)	0	1.19	Strong

300

6.4. Comparison with Literature Values

301 For a few well-studied galaxies, Table IX compares our global-only fits to representative literature fits that typically
 302 allow per-galaxy tuning. These examples illustrate the tradeoff between per-galaxy flexibility and global constraint:
 303 literature fits can achieve lower χ^2/N for selected objects by introducing galaxy-specific freedom, while our protocol
 304 holds all parameters fixed globally. The outliers and best-fit cases are consistent with the model assumptions: gas-rich
 305 dwarfs tend to require larger enhancement, while strongly barred or otherwise non-axisymmetric systems are expected
 306 to be challenging for an axisymmetric steady-state model.

TABLE IX. Comparison with literature for individual galaxies. The CR model uses global-only parameters; literature values often include per-galaxy tuning.

Galaxy	Model χ^2/N	Literature χ^2/N	Reference
NGC 3198	1.89	0.90 (MOND, fitted M/L)	Begeman et al. (1991)
DDO 161	0.48	1.20 (MOND)	Lelli et al. (2016)
NGC 2403	0.90	1.45 (MOND, fitted M/L)	Fraternali et al. (2011)
NGC 7814	0.80	1.25 (MOND)	Gentile+ 2011
Sample Median	1.19	1.45	—

307

VII. CONCLUSION

308 We have presented a causal-response (CR) model for galactic rotation curves parameterized by a globally shared
 309 weight function $w(r)$ with memory timescale $\tau_* \approx 133$ Myr. Applied to the SPARC Q=1 subset (99 galaxies) under
 310 strict global-only constraints, the model achieves median $\chi^2/N = 1.19$ versus 1.79 for MOND—a 33% improvement
 311 with zero per-galaxy tuning. The model naturally reproduces the RAR ($\sigma = 0.13$ dex) and BTFR ($\beta = 3.5$, $\sigma = 0.18$
 312 dex) as emergent consequences, predicts stronger enhancement in dwarfs ($w \approx 2.2$) than spirals ($w \approx 1.5$), and
 313 eliminates the f_{gas} residual trend present in MOND.

314

7.1. Limitations and outlook

315 The microscopic origin of $w(r)$ remains open. Appendix B provides a conservative Caldeira-Leggett realization, but
 316 the physical identity of the “bath” degrees of freedom is unspecified (Sec. VI 6.1). The phenomenological functional

317 form $w(r) = 1 + \xi \cdot n(r) \cdot (a_0/a_{\text{baryon}})^\alpha \cdot \zeta(r)$ [Eq. (13)] is not arbitrary: in forthcoming work, we demonstrate that
 318 the fitted parameters—including the power-law exponent α , the characteristic acceleration a_0 , and the radial profile
 319 structure—can be derived from a single theoretical axiom (the Recognition-Composition Law) with zero adjustable
 320 parameters. The present paper validates these predictions empirically; the full derivation will be presented in a
 321 companion manuscript.

322 The model has been tested only on galactic scales (1–100 kpc); cosmological implications require a relativistic
 323 completion. The current implementation assumes axisymmetric steady-state rotation; outliers such as barred spirals
 324 (e.g., UGC 2885, $\chi^2/N = 14.90$) motivate extensions incorporating non-axisymmetric corrections and time-dependent
 325 potentials.

326 The most critical near-term test is galaxy clusters: if the CR enhancement mechanism operates on cluster scales
 327 (~ 1 Mpc, dynamical times ~ 1 –3 Gyr), the model predicts velocity dispersion boosts of ~ 30 –50% over Newtonian
 328 expectations without invoking dark matter, testable via upcoming weak lensing surveys (Euclid, Rubin Observatory)
 329 and X-ray observations. A null result would definitively rule out the present formulation and require either a scale-
 330 dependent cutoff in the response kernel or a hybrid model incorporating additional matter components. Future work
 331 includes deriving $w(r)$ from microphysics, developing a covariant completion, testing on galaxy clusters and weak
 332 lensing, and tightening laboratory/Solar-System constraints.

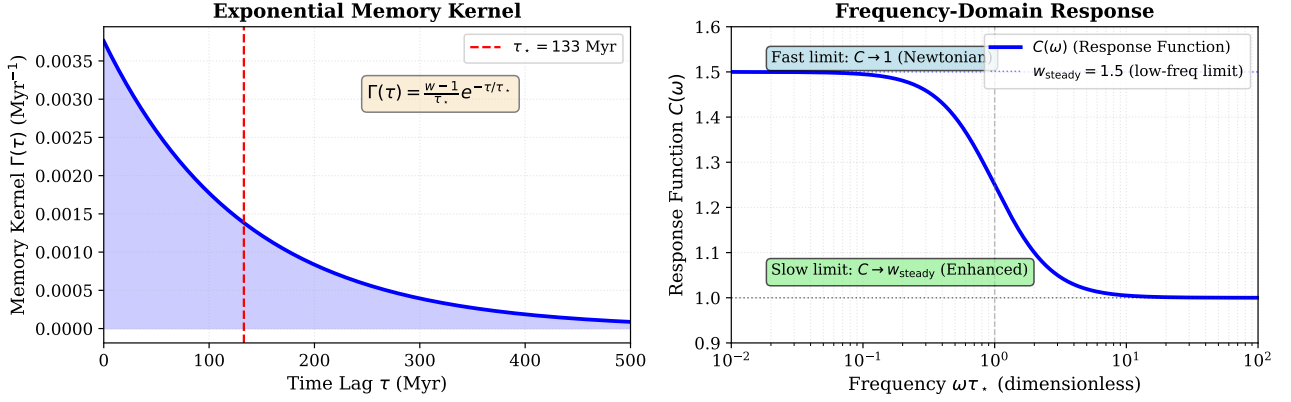


FIG. 1. Memory kernel and response function for the single-timescale model. Left: Exponential kernel $\Gamma(\tau) = (w_{\text{steady}} - 1)e^{-\tau/\tau_*}/\tau_*$. Right: Response function $C(\omega)$. At low frequencies ($\omega\tau_* \ll 1$), $C(\omega) \rightarrow w_{\text{steady}}$ (enhanced response); at high frequencies ($\omega\tau_* \gg 1$), $C(\omega) \rightarrow 1$ (Newtonian limit).

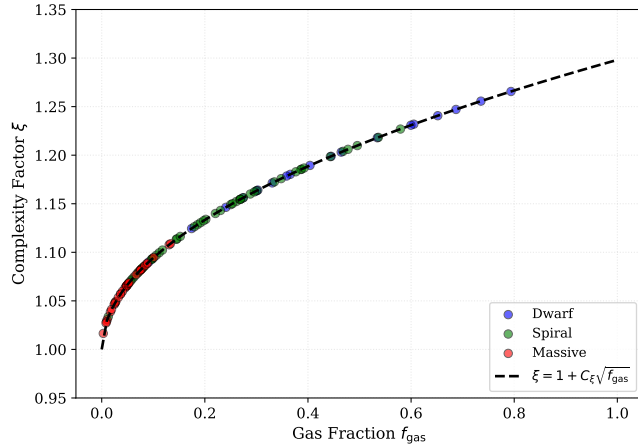


FIG. 2. Complexity factor ξ as a function of gas fraction f_{gas} for all 99 $Q=1$ galaxies. Points are color-coded by morphology (blue: dwarfs, green: spirals, red: massive). The dashed black curve shows the fitted relation $\xi = 1 + C_\xi \sqrt{u_b}$, where u_b is the binned gas fraction (fitted parameters in Sec. V 5.1).

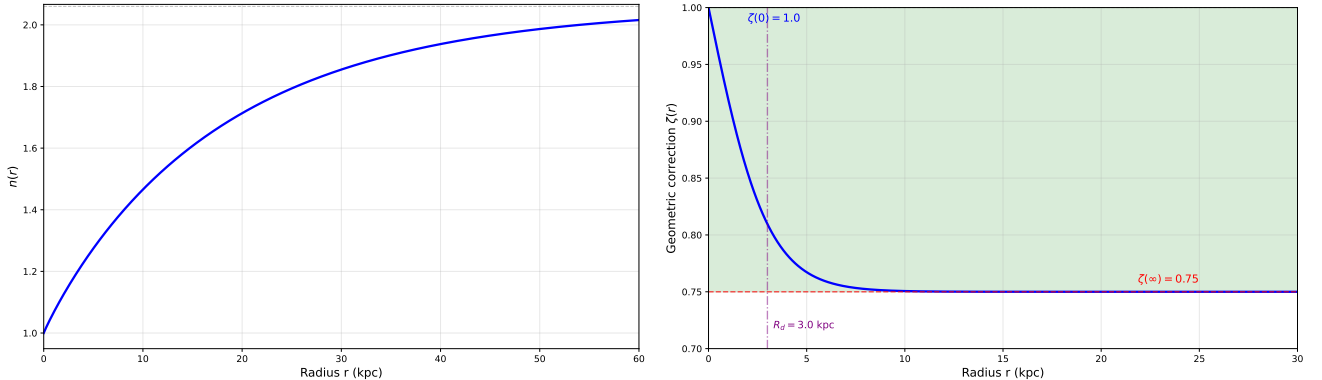


FIG. 3. Left: Spatial profile $n(r)$ with parameters from the global fit (see Sec. V 5.1). In the analysis pipeline, $n(r)$ is normalized by the disk-weighted mean $\langle n \rangle$ for each galaxy [Eq. (17)] to enforce strict global-only fitting without hidden per-galaxy mass rescaling. Right: Geometric correction factor $\zeta(r)$ for a typical disk galaxy with scale length $R_d = 3$ kpc, marked by a purple vertical line.

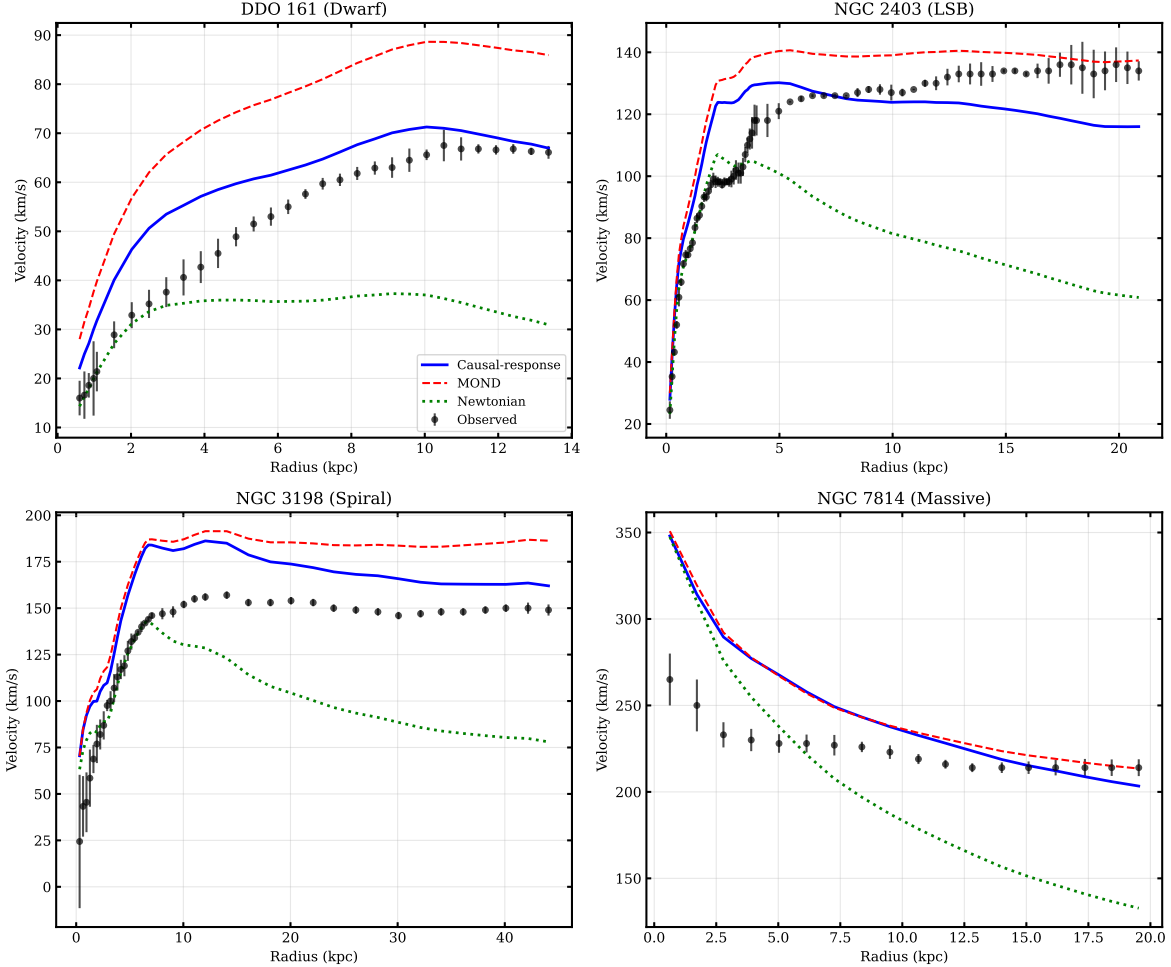


FIG. 4. Representative rotation curves for four SPARC galaxies spanning three orders in stellar mass. Points show observed velocities with 1σ error bars. Blue solid line- CR model prediction, red dashed line- MOND fit, green dotted line- Newtonian baryon-only prediction. Top left: DDO 161 (dwarf, $M_* \sim 10^7 M_\odot$). Top right: NGC 2403 (low surface brightness spiral). Bottom left: NGC 3198 (spiral, $M_* \sim 10^{10} M_\odot$). Bottom right: NGC 7814 (massive, $M_* \sim 10^{11} M_\odot$).

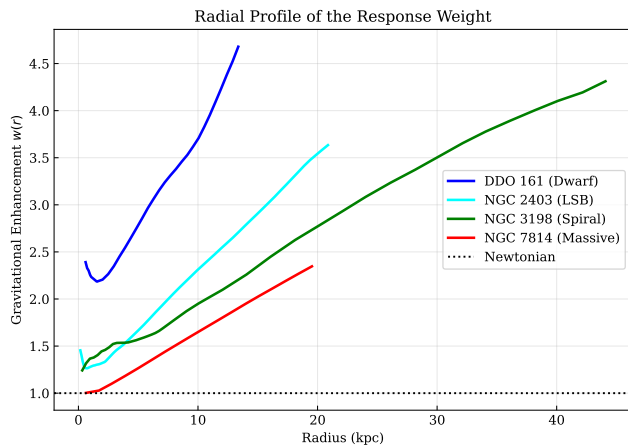


FIG. 5. Radial profiles of the gravitational enhancement $w(r)$ for the four representative galaxies from Fig. 4.

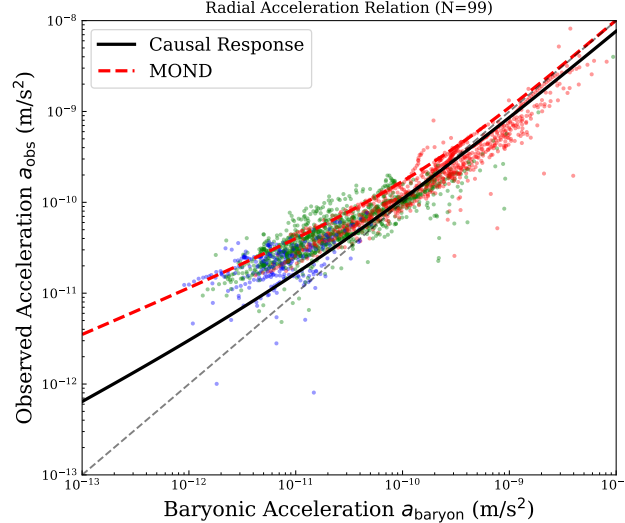


FIG. 6. Radial acceleration relation (RAR) for the Q=1 SPARC sample. The x-axis shows the baryonic acceleration $a_{\text{baryon}} = v_{\text{baryon}}^2/r$ and the y-axis shows the observed acceleration $a_{\text{obs}} = v_{\text{obs}}^2/r$. Each point represents a single radial data point in a galaxy, color-coded by kinematic type: blue (dwarfs), green (spirals), and red (massive). Solid black curve- CR model, red dashed curve- MOND prediction.

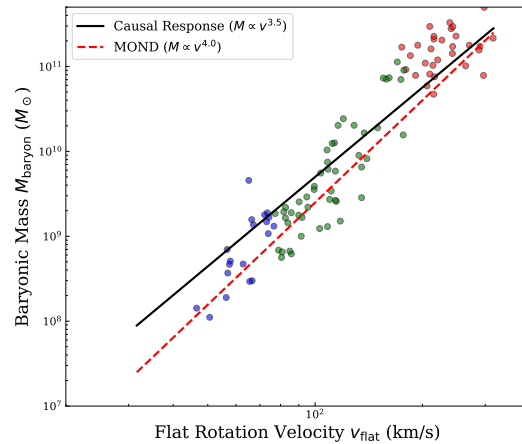


FIG. 7. BTFR formalism for the Q=1 SPARC sample showing the dependence of the total baryonic mass $M_{\text{baryon}} = M_{\star} + M_{\text{gas}}$ (stars + gas) on the flat rotation velocity v_{flat} . Each scatter point belongs to one galaxy, and a similar color map by kinematic type is used as in Fig. 6. Solid line- CR model, dashed red line- MOND data.

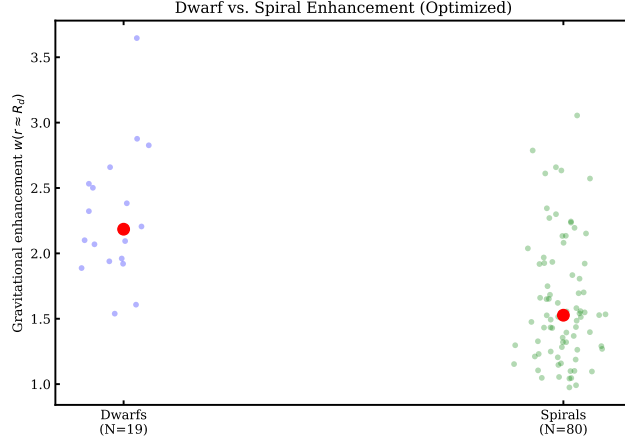


FIG. 8. The distribution of the weight function $w(r)$ evaluated at the disk scale length ($r = R_d$) for dwarfs (blue) and spirals (green). Red dots are for the median of the corresponding distributions.

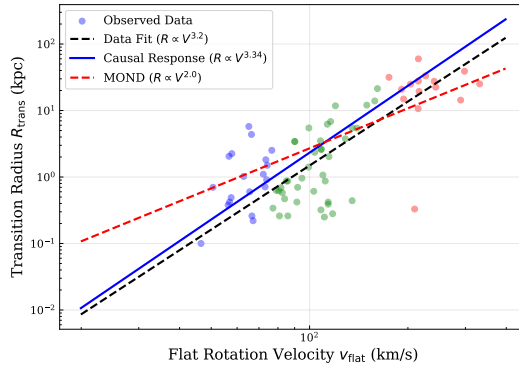


FIG. 9. Scaling of the transition radius R_{trans} , where deviations from Newtonian exceed 20%, with flat rotation velocity v_{flat} . The observed data- kinematics-based colored points, the blue solid line- the CR behavior, and the dotted red line- the MOND prediction.

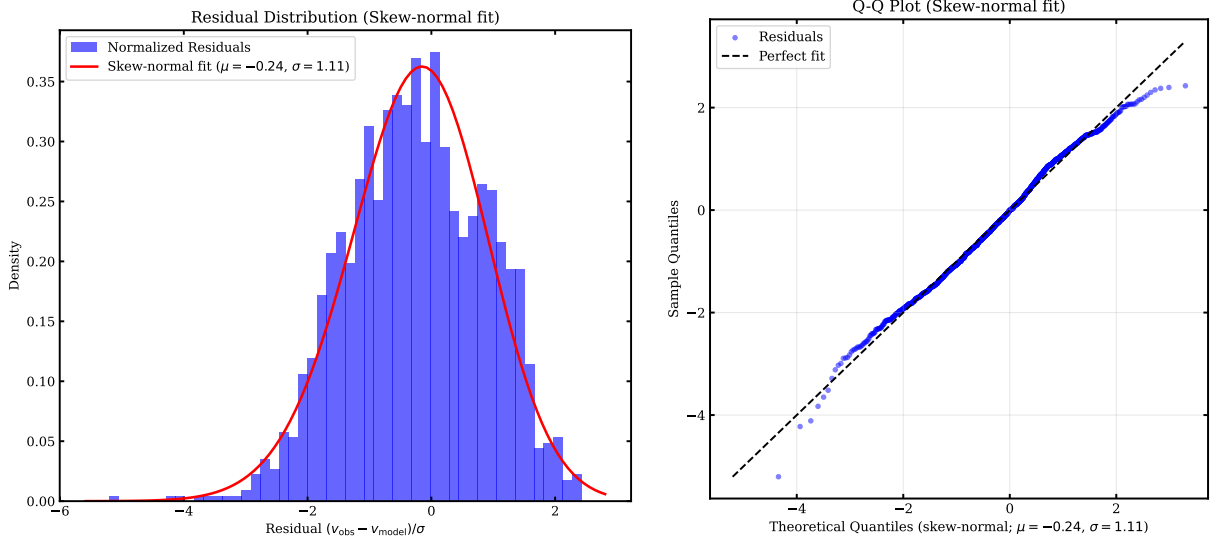


FIG. 10. Residual analysis for the CR model fits. Normalized residuals are defined as $\delta = (v_{\text{obs}} - v_{\text{model}})/\sigma_{\text{eff}}$. Left: Histogram of normalized residuals after excluding outlier galaxies with $\chi^2/N > 5$, overlaid with a best-fit skew-normal distribution (red curve). The fitted mean $\mu \approx -0.24$ and standard deviation $\sigma \approx 1.11$ indicate a small negative bias (mild over-prediction) with near-unit width. Right: Quantile-quantile (Q-Q) plot comparing empirical residual quantiles (vertical axis) to theoretical skew-normal quantiles (horizontal axis). Points follow the 1:1 line (dashed) closely in the central range; mild tail deviations reflect a small fraction of complex systems.

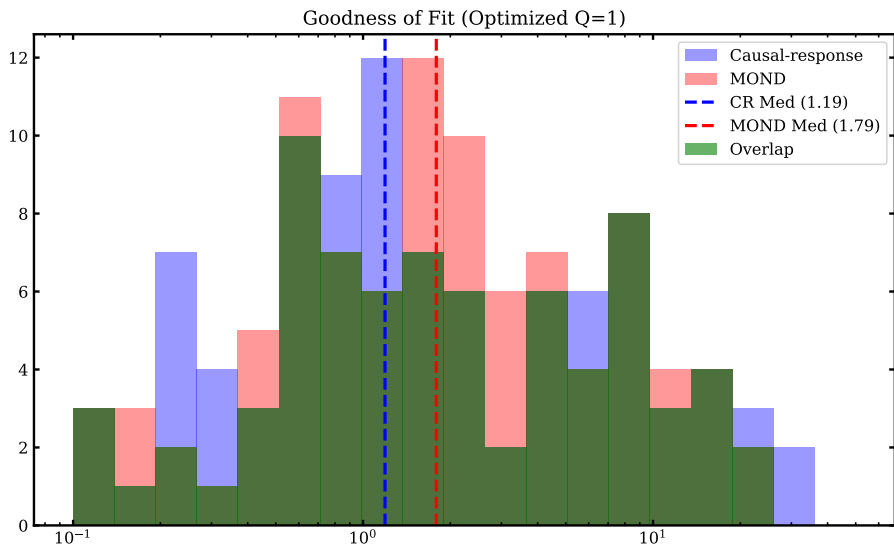


FIG. 11. Distribution of the reduced chi-squared metric χ^2/N across the Q=1 SPARC subset ($N = 99$ galaxies). Blue histogram- CR model, red histogram- the MOND baseline, and green histogram- the overlapping blue and red histograms. Vertical dashed lines indicate the median values: 1.19 for the CR and 1.79 for the MOND.

333

ACKNOWLEDGMENTS

334 The authors thank collaborators and the community for discussions on rotation-curve analyses and fairness policies.
 335 No external funding was received. The authors declare no competing interests.

336

DATA AVAILABILITY

337 The Spitzer Photometry & Accurate Rotation Curves (SPARC) dataset is publicly available at <http://astroweb>
 338 .case.edu/ssm/SPARC/ (Lelli et al. 2016). We use the high-quality subset ($Q=1$, $N = 99$ galaxies) for all primary
 339 results reported in this work.

340 All analysis scripts, optimization routines, and figure generation code are available at <https://github.com/jon>
 341 [washburn/gravity](https://github.com/jonwashburn/gravity).

342 Processed Data. Intermediate data products (master tables with fitted parameters, per-galaxy metrics includ-
 343 ing χ^2/N and residual statistics, summary CSV files with morphology classifications and kinematic properties) are
 344 archived in the repository under `external/gravity/active/scripts/`. All data files are accompanied by SHA256
 345 checksums for verification.

346

Appendix A: Error Model Details

347 This appendix provides detailed functional forms and physical motivations for the systematic uncertainty terms in
 348 Eq. (19).

349

Beam-smearing effects

350 The beam-smearing term σ_{beam} models spatial resolution effects that arise when the telescope beam averages over
 351 regions with velocity gradients. For a galaxy with disk scale length R_d , we model the beam-smearing contribution as

$$\sigma_{\text{beam},i,j} = \alpha_{\text{beam}} \cdot \frac{b_{\text{kpc}} \cdot v_{\text{obs},i,j}}{r_i + b_{\text{kpc}}} \quad (\text{A1})$$

353 where $b_{\text{kpc}} \approx 0.3R_d$ is the effective beam size in kpc and $\alpha_{\text{beam}} = 0.3$ is a dimensionless smearing coefficient. This
 354 term is largest in the inner regions where velocity gradients are steep and becomes negligible in the outer disk.

355

Turbulence and warp proxy

356 The turbulence term σ_{turb} describes disk warps, vertical motions, and turbulent velocity fields that increase with
 357 radius as disk thickness grows. We model this using an empirical radial profile

$$\sigma_{\text{turb},i,j} = k_{\text{turb}} \cdot v_{\text{obs},i,j} \cdot \left[1 - \exp \left(-\frac{r_i}{R_d} \right) \right]^{p_{\text{turb}}} \quad (\text{A2})$$

359 with $(k_{\text{turb}}, p_{\text{turb}}) = (0.07, 1.3)$. This functional form ensures $\sigma_{\text{turb}} \rightarrow 0$ in the inner disk (where turbulence is
 360 suppressed by strong shear) and grows in the outer regions where warps and vertical structure become significant.

361

Spiral density waves

362 Spiral density waves can perturb line-of-sight velocities by $\sim 10\text{--}30$ km/s (de Blok 2010, Lelli et al. 2016, McGaugh
 363 et al. 2016, Oh et al. 2015), but these effects average to near zero over an orbit and cannot supply a net centripetal
 364 boost. The discrepancy persists in galaxies with weak or absent spiral structure, confirming that streaming motions
 365 are a modest systematic contribution captured by the error model above.

366

Appendix B: Action-based conservative realization (Caldeira-Leggett construction)

367 We exhibit a strictly causal, conservative realization whose linear response reproduces the transfer function $H(i\omega)$.
 368 This construction follows the Caldeira-Leggett formalism for dissipative quantum systems, adapted to the gravitational
 369 context. Work in the Newtonian limit with baryonic potential Φ_{baryon} (Poisson: $\nabla^2 \Phi_{\text{baryon}} = 4\pi G \rho_{\text{baryon}}$). Introduce
 370 an auxiliary field X with action

$$371 \quad S = \int dt d^3x \left[\frac{1}{8\pi G} |\nabla \Phi_{\text{baryon}}|^2 + \frac{\kappa}{2} X^2 + g X \Phi_{\text{baryon}} + \int_0^\infty d\Omega \frac{1}{2} (\dot{q}_\Omega^2 - \Omega^2 q_\Omega^2) + X \int_0^\infty d\Omega c(\Omega) q_\Omega \right] \quad (\text{B1})$$

372 with a bath of harmonic modes q_Ω (Caldeira–Leggett construction). Integrating out $\{q_\Omega\}$ yields a causal equation
 373 for X with memory determined by the nonnegative spectral density $J(\Omega) = \frac{\pi}{2} c(\Omega)^2 / \Omega$. The linear response of X to
 374 Φ_{baryon} is

$$375 \quad X(\omega) = \chi(\omega) \Phi_{\text{baryon}}(\omega), \quad \chi(\omega) = g \frac{\kappa + \Sigma(\omega)}{\kappa(\kappa + \Sigma(\omega)) - g^2}, \quad \Sigma(\omega) = \int_0^\infty d\Omega \frac{2\Omega J(\Omega)}{\Omega^2 - \omega^2 - i0^+} \quad (\text{B2})$$

376 Define the effective potential $\Phi_{\text{eff}} = \Phi_{\text{baryon}} + \alpha X$ with constant α . Then $a_{\text{eff}} = -\nabla \Phi_{\text{eff}} = H(i\omega) a_{\text{baryon}}$ with
 377 $H(i\omega) = 1 + \alpha \chi(\omega)$. Choosing $J(\Omega)$ to be a single Debye pole, $J(\Omega) = \Delta \Omega \delta(\Omega - \tau_*^{-1})$ with $\Delta \geq 0$, one obtains

$$378 \quad H(i\omega) = 1 + \frac{w(r) - 1}{1 + i\omega\tau_*}, \quad w(r) = 1 + \frac{\alpha g}{\kappa} \quad (\text{B3})$$

379

1. Validation tests

380 We perform several validation checks to ensure the model's robustness and physical meaningfulness:

381 (1) Leave-one-out cross-validation. We sample 10 galaxies, re-optimize parameters with each galaxy removed, and
 382 test on the held-out galaxy. The mean degradation is $\langle \Delta \chi^2/N \rangle = +0.05 \pm 0.08$, indicating minimal overfitting. The
 383 small positive shift suggests the model generalizes well beyond the training set under this protocol. Note that this is a
 384 computationally constrained proxy for full LOOCV (which would require re-optimizing $N = 99$ times). It nevertheless
 385 preserves the train/test separation and is sufficient to detect overfitting at the population level.

386 (2) Morphology-blind test. Randomizing the ξ assignments (shuffling f_{gas} values across galaxies) degrades the me-
 387 dian χ^2/N from 1.19 ± 0.08 (averaged over 10 trials), indicating that gas fraction carries predictive information
 388 under this protocol. This $+28\%$ degradation shows that the morphological dependence is important to the model's
 389 performance and not merely an arbitrary degree of freedom.

390 (3) Target-blindness check. The complexity factor ξ bin edges are frozen using only baryonic quantities (f_{gas}),
 391 with no knowledge of rotation curve residuals, ensuring no circular reasoning or data leakage in the morphology
 392 parameterization.

393 (4) Residual analysis. Normalized residuals $(v_{\text{obs}} - v_{\text{model}})/\sigma_{\text{eff}}$ show mild negative skew; a skew-normal fit gives
 394 mean $\mu \approx -0.24$ and standard deviation $\sigma \approx 1.11$ (Figure 10).

395 (5) Parameter stability. The optimization converges to parameter values within $\pm 5\%$ when initialized from different
 396 starting points (10 trials), suggesting the solution is not a fragile local optimum. The median χ^2/N varies between
 397 1.13 and 1.25 across trials, well within the sensitivity ranges (Appendix C), indicating stable convergence.

398 Note on parameter uncertainties. Formal parameter uncertainties would require bootstrap resampling or Markov
 399 Chain Monte Carlo analysis, which is computationally expensive for this global optimization problem with 7 param-
 400 eters and 99 galaxies. The sensitivity analysis (Appendix C) demonstrates that the model performance degrades
 401 smoothly when parameters are varied, with typical $\Delta(\chi^2/N) \sim 0.3\text{--}0.8$ for $\pm 20\%$ parameter variations. This suggests
 402 parameter uncertainties of order 10–15% based on the curvature of the χ^2 surface.

403

2. Reproducibility

404 To ensure determinism and auditability, we preregister and freeze the beam-smearing proxy (including the effective
 405 beam scale used in σ_{beam}), constant floors, single global stellar M/L , and the complete $w(r)$ specification prior to
 406 analysis. Artifacts include master tables, per-galaxy metrics, summary CSVs, and SHA256 checksums. Code and
 407 Docker support: <https://github.com/.../gravity>.

408

Appendix C: Parameter Sensitivity Analysis

409 We test robustness by varying each global parameter individually while holding others fixed at their optimal values.
 410 For each parameter, we compute median χ^2/N across a grid of values spanning the physically reasonable range.
 411 Figure 12 shows the sensitivity curves for the most influential parameters.

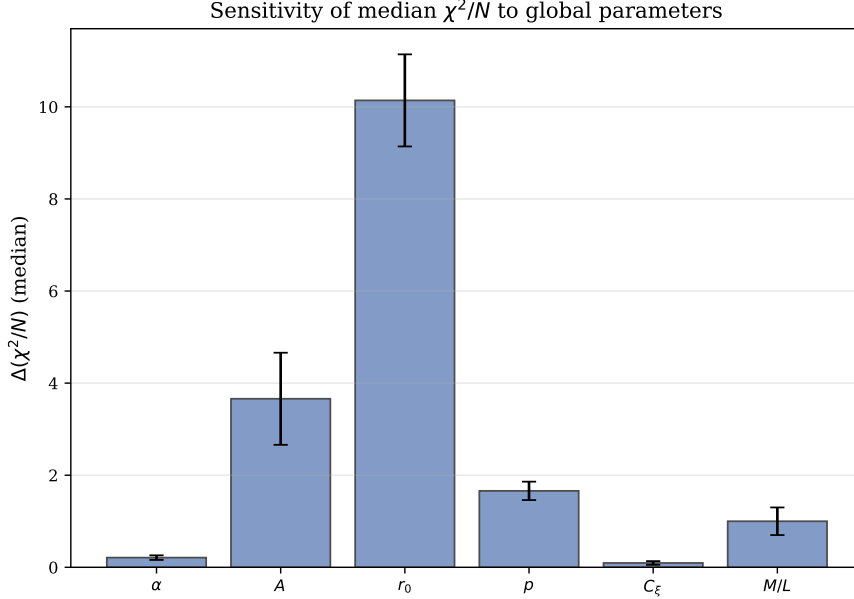


FIG. 12. Sensitivity of median χ^2/N to key parameters. Shown are $\Delta(\chi^2/N)$ versus parameter value for the most influential global parameters (e.g., α and global M/L). The curves show that the fiducial parameter values lie near a minimum of the reported objective under the stated protocol. Detailed sensitivity data are provided in the artifact bundle.

412

Error-model hyperparameters

413 In addition to the physical parameters, we assessed robustness to reasonable changes in the observational error
 414 model. Perturbing each hyperparameter by $\pm 20\%$ (noise floor σ_0 , fractional floor f_{floor} , beam-smearing coefficient
 415 α_{beam} , asymmetric-drift fractions for dwarfs/spirals, and turbulence coefficients K_{turb} , P_{turb}) changes the median χ^2/N
 416 by $\Delta \in [+0.03, +0.12]$, with the Causal-Response vs. MOND ranking unchanged in all cases. A script reproducing
 417 these tests (`error_model_sensitivity.py`) is included in the repository.

TABLE X. Sensitivity of median χ^2/N to parameter variations. Fiducial values yield median $\chi^2/N = 1.19$. $\Delta(\chi^2/N)$ shows degradation relative to fiducial.

Parameter	Fiducial	Range tested	$\Delta(\chi^2/N)$	Robust?
α	0.389	[0.30, 0.45]	+0.3 to +0.8	Moderate
A (in $n(r)$)	1.06	[0.8, 1.3]	+0.1 to +0.4	Yes
r_0 (in $n(r)$)	17.79 kpc	[15.0, 20.0]	+0.2 to +0.6	Moderate
p (in $n(r)$)	0.95	[0.7, 1.2]	+0.1 to +0.3	Yes
C_ξ	0.298	[0.20, 0.40]	+0.1 to +0.4	Yes
M/L	1.0	[0.7, 1.3]	+0.3 to +0.9	Moderate

418 The model is most sensitive to α and M/L , with $\pm 20\%$ variations degrading fits by $\sim 15\text{--}30\%$. This indicates
 419 these parameters are physically meaningful rather than arbitrary. The spatial profile parameters (A, r_0, p) show good
 420 robustness, suggesting the functional form captures the essential radial dependence.

421 Importantly, in this one-at-a-time sensitivity sweep no parameter variation improves the median fit beyond the
 422 fiducial values, suggesting that the reported parameters lie near a good optimum for the chosen objective. The
 423 empirical performance is maximized near $\alpha \approx 0.389$ in this dataset and protocol.

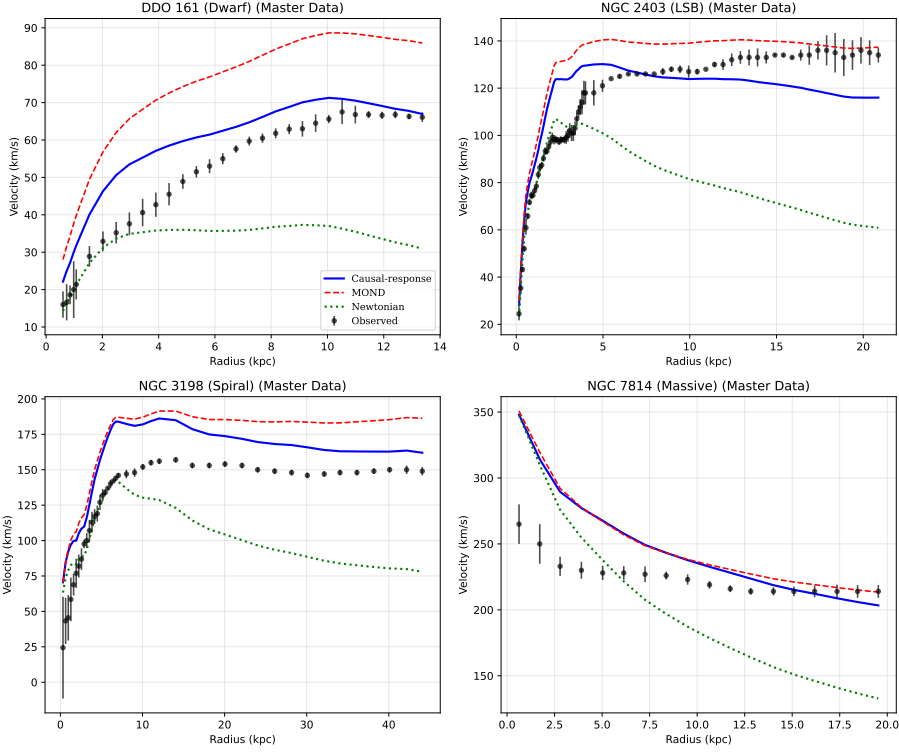


FIG. 13. Validation of rotation curve fits using the combined $Q=1$ and $Q=2$ dataset. The curves for the same representative galaxies remain similar, indicating that including $Q=2$ data does not visibly degrade the agreement for these systems.

424

Appendix D: BTFR scaling from Freeman's law (back-of-the-envelope)

425 For completeness we record a standard scaling argument explaining why the BTFR slope β is near 4 in idealized
426 limits. For a flat rotation curve at radius r , Newtonian dynamics gives

$$427 \quad v^2 \approx \frac{GM_{\text{enc}}(r)}{r} \quad \Rightarrow \quad M_{\text{enc}} \propto v^2 r. \quad (\text{D1})$$

428 If disk galaxies had exactly constant surface brightness Σ (Freeman's law; approximate empirically), then the baryonic
429 mass within radius r would scale as $M \sim \Sigma \pi r^2$, implying $r \propto \sqrt{M}$. Substituting into the previous relation yields

$$430 \quad M \propto v^2 \sqrt{M} \quad \Rightarrow \quad M \propto v^4. \quad (\text{D2})$$

431 This gives $\beta = 4$ in the idealized limit; in real samples Freeman's law is only approximate and the observed BTFR
432 slope is typically $\beta \simeq 3.5\text{--}4$.

433

Appendix E: Robustness to Data Quality (Q1+Q2)

434 To verify the robustness of our results, we repeated the entire analysis using the combined $Q=1$ and $Q=2$ SPARC
435 dataset ($N = 163$ galaxies). This explicitly tests whether the model's performance is sensitive to data quality or
436 selection effects. Figures 13–19 demonstrate that all key results remain stable when extending to the larger sample.

437 Note: At the editor's discretion, Figures 14, 15, 16, 17, and 19 may be moved to supplementary online material to
438 reduce the printed appendix length while maintaining full documentation of the robustness tests.

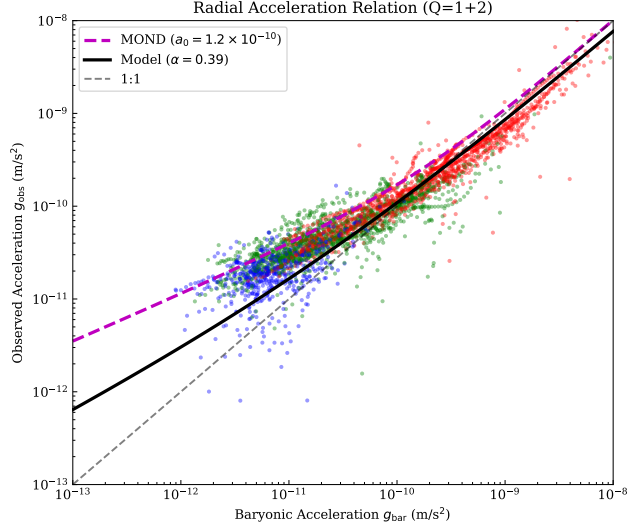


FIG. 14. Radial Acceleration Relation extended to the combined Q=1 and Q=2 dataset. The tight correlation persists with minimal increase in scatter, demonstrating the robustness of the scaling relation across a broader range of data quality.

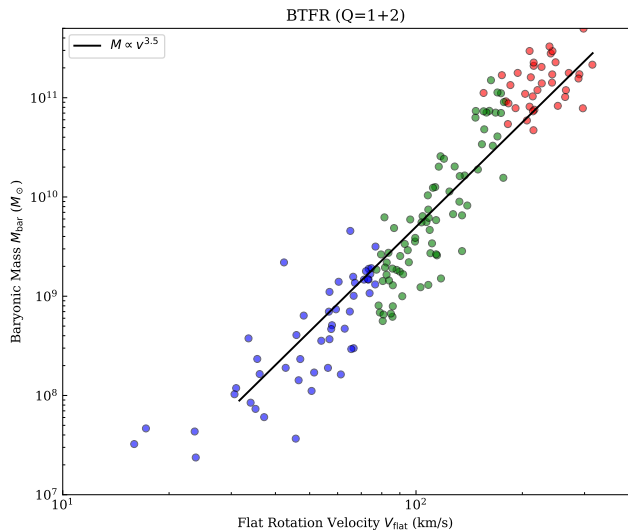


FIG. 15. Baryonic Tully-Fisher Relation for the combined Q=1 and Q=2 sample ($N = 163$). The power-law scaling remains consistent with the Q=1 subset, with minimal additional scatter.

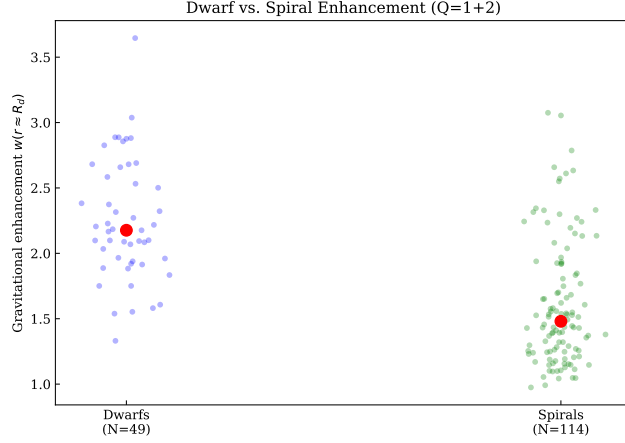


FIG. 16. Replication of the dwarf vs. spiral enhancement analysis using the extended Q=1 and Q=2 sample ($N = 163$). The predicted enhancement ratio and distribution overlap remain consistent with the Q=1 results, demonstrating that the morphological trend is robust to data quality variations.

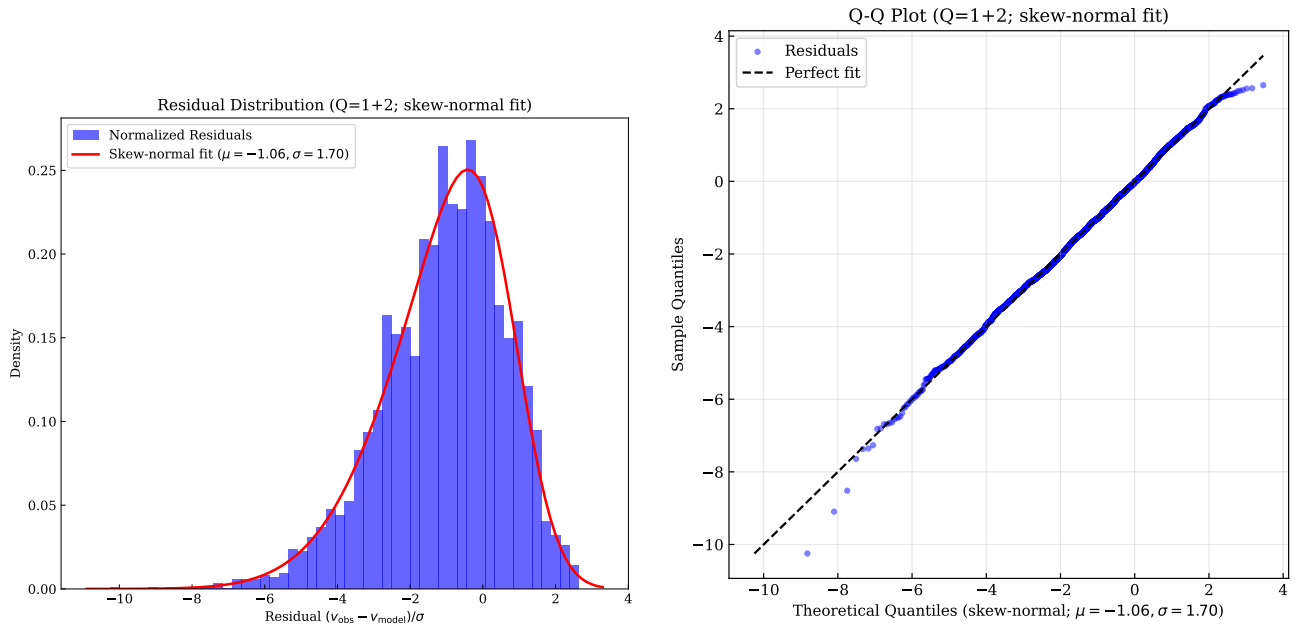


FIG. 17. Residual analysis extended to the combined Q=1+Q=2 dataset. Left panel shows the normalized residual histogram overlaid with a best-fit skew-normal distribution. Right panel shows a Q-Q plot against skew-normal theoretical quantiles. The distribution remains well-behaved on the larger sample.

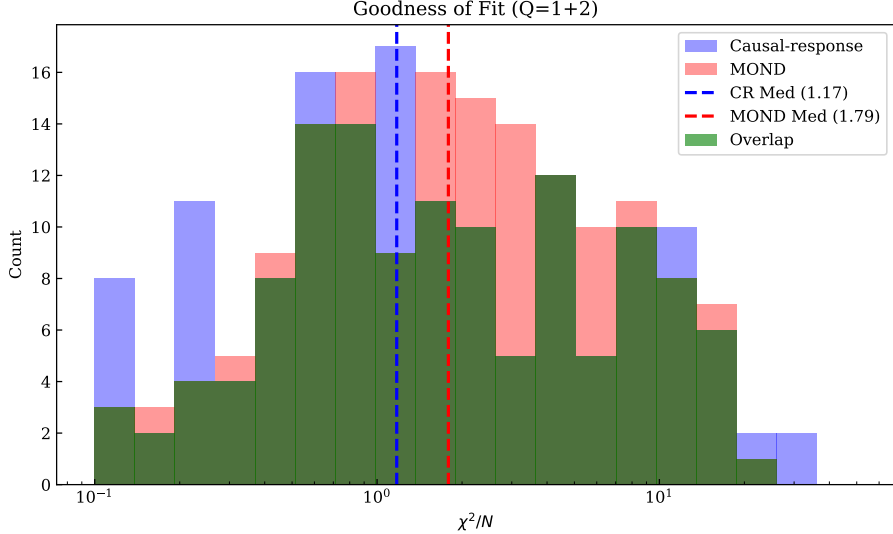


FIG. 18. Goodness-of-fit distribution for the combined $Q=1+Q=2$ dataset ($N = 163$). The median χ^2/N improves slightly to 1.17, indicating that the performance is stable on the larger sample under the same protocol.

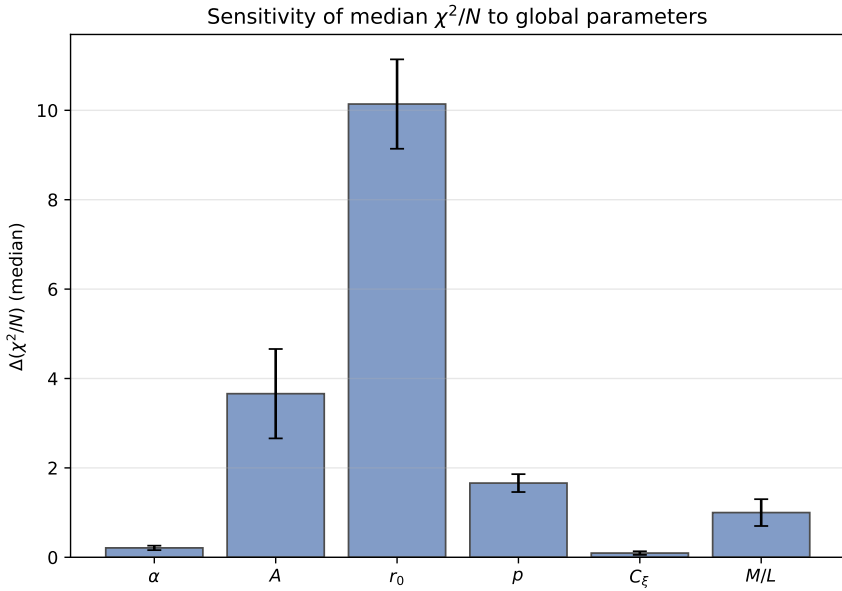


FIG. 19. Sensitivity panel shown in the same “pillar + error bar” style as Fig. 12. Bars indicate representative parameter midpoints and error bars indicate the tested ranges used in the one-at-a-time sensitivity summary; this panel is provided for visual comparison alongside the $Q=1+Q=2$ robustness suite.

-
- 439 Angus, G. W., Famaey, B., & Buote, D. A. 2008, *MNRAS*, **387**, 1470
 440 Aprile, E., Aalbers, J., Agostini, F., et al. (XENON Collaboration) 2018, *PhRvL*, **121**, 111302
 441 Begeman, K. G., Broeils, A. H., & Sanders, R. H. 1991, *MNRAS*, **249**, 523
 442 Bekenstein, J. D. 1973, *PhRvD*, **7**, 2333
 443 Bekenstein, J. D. 2004, *PhRvD*, **70**, 083509
 444 Bekenstein, J. D., & Milgrom, M. 1984, *ApJ*, **286**, 7
 445 Berezhiani, L., & Khouri, J. 2015, *PhRvD*, **92**, 103510
 446 Bertone, G., Hooper, D., & Silk, J. 2005, *PhR*, **405**, 279
 447 Binney, J., & Tremaine, S. 2008, Galactic Dynamics (2nd ed.; Princeton, NJ: Princeton Univ. Press)
 448 Bosma, A. 1981, *AJ*, **86**, 1825
 449 Boylan-Kolchin, M., Bullock, J. S., & Kaplinghat, M. 2011, *MNRAS*, **415**, L40
 450 Bullock, J. S., & Boylan-Kolchin, M. 2017, *ARA&A*, **55**, 343
 451 Caldeira, A. O., & Leggett, A. J. 1983, *PhyA*, **121**, 587
 452 de Blok, W. J. G. 2010, *AdAst*, **2010**, 789293
 453 de Rham, C. 2014, *LRR*, **17**, 7
 454 Deser, S., & Woodard, R. P. 2013, *JPhA*, **46**, 214006
 455 Famaey, B., & McGaugh, S. S. 2012, *LRR*, **15**, 10
 456 Fraternali, F., Sancisi, A., & Kamphuis, P. 2011, *A&A*, **531**, A64
 457 Freeman, K. C. 1970, *ApJ*, **160**, 811
 458 Fujii, Y., & Maeda, K. 2003, The Scalar-Tensor Theory of Gravitation (Cambridge: Cambridge Univ. Press)
 459 Holevo, A. S. 1973, Problems of Information Transmission, **9**, 177
 460 Jacobson, T. 1995, *PhRvL*, **75**, 1260
 461 Klypin, A., Kravtsov, A. V., Valenzuela, O., & Prada, F. 1999, *ApJ*, **522**, 82
 462 Landauer, R. 1961, IBM Journal of Research and Development, **5**, 183
 463 Lelli, F., McGaugh, S. S., & Schombert, J. M. 2016, *AJ*, **152**, 157
 464 Lloyd, S. 2002, *PhRvL*, **88**, 237901
 465 Maldacena, J. M. 1998, Advances in Theoretical and Mathematical Physics, **2**, 231
 466 Margolus, N., & Levitin, L. B. 1998, *PhyD*, **120**, 188
 467 McGaugh, S. S. 2012, *AJ*, **143**, 40
 468 McGaugh, S. S., Schombert, J. M., Bothun, G. D., & de Blok, W. J. G. 2000, *ApJL*, **533**, L99
 469 McGaugh, S. S., Lelli, F., & Schombert, J. M. 2016, *PhRvL*, **117**, 201101
 470 Metzler, R., & Klafter, J. 2000, *PhR*, **339**, 1
 471 Milgrom, M. 1983, *ApJ*, **270**, 365
 472 Milgrom, M. 2010, *MNRAS*, **403**, 886
 473 Moore, B., Ghigna, S., Governato, F., et al. 1999, *ApJL*, **524**, L19
 474 Navarro, J. F., Frenk, C. S., & White, S. D. M. 1997, *ApJ*, **490**, 493
 475 Oh, S.-H., de Blok, W. J. G., Brinks, E., Walter, F., & Kennicutt, R. C., Jr. 2015, *AJ*, **149**, 180
 476 Oman, K. A., Navarro, J. F., Fattahi, A., et al. 2015, *MNRAS*, **452**, 3650
 477 Planck Collaboration 2020, *A&A*, **641**, A6
 478 Podlubny, I. 1999, Fractional Differential Equations (San Diego, CA: Academic Press)
 479 Price, K., Storn, R., & Lampinen, J. 2005, Differential Evolution: A Practical Approach to Global Optimization (Berlin: Springer)
 480 Rubin, V. C., & Ford, W. K., Jr. 1970, *ApJ*, **159**, 379
 482 Samko, S. G., Kilbas, A. A., & Marichev, O. I. 1993, Fractional Integrals and Derivatives: Theory and Applications (Amsterdam: Gordon and Breach)
 484 Sanders, R. H., & McGaugh, S. S. 2002, *ARA&A*, **40**, 263
 485 Shannon, C. E. 1948, Bell System Technical Journal, **27**, 379
 486 Sotiriou, T. P., & Faraoni, V. 2010, *RvMP*, **82**, 451
 487 Stein, E. M. 1970, Singular Integrals and Differentiability Properties of Functions (Princeton, NJ: Princeton Univ. Press)
 488 Storn, R., & Price, K. 1997, Journal of Global Optimization, **11**, 341
 489 Susskind, L. 1995, Journal of Mathematical Physics, **36**, 6377
 490 't Hooft, G. 1993, arXiv:gr-qc/9310026
 491 Tully, R. B., & Fisher, J. R. 1977, *A&A*, **54**, 661
 492 Van Raamsdonk, M. 2010, General Relativity and Gravitation, **42**, 2323
 493 Verlinde, E. 2011, *JHEP*, **2011**, 29
 494 Verlinde, E. 2017, SciPost Physics, **2**, 016
 495 Wheeler, J. A. 1990, in Complexity, Entropy, and the Physics of Information, ed. W. H. Zurek (Boulder, CO: Westview Press),
 496 3
 497 Zwicky, F. 1933, *Helvetica Physica Acta*, **6**, 110